Comparative Assessment of Some Target Detection Algorithms for Hyperspectral Images

Manoj K. Arora, Shweta Bansal, Sangeeta Khare[*#], and Kiran Chauhan[#]

Indian Institute of Technology Roorkee, Roorkee - 247 667, India
#Defence Electronics Applications Laboratory, Dehradun - 248 001, India
*E-mail: sangeeta_kharey@yahoo.co.in

ABSTRACT

Target detection is of particular interest in hyperspectral image analysis as many unknown and subtle signals (spectral response) unresolved by multispectral sensors can be discovered in hyperspectral images. The detection of signals in the form of small objects and targets from hyperspectral sensors has a wide range of applications both civilian and military. It has been observed that a number of target detection algorithms are in vogue; each has its own advantages and disadvantages and assumptions. The selection of a particular algorithm may depend on the amount of information available as per the requirement of the algorithm, application area, the computational complexity etc. In the present study, three algorithms, namely, orthogonal subspace projection (OSP), constrained energy minimization (CEM) and a nonlinear version of OSP called kernel orthogonal subspace projection (KOSP), have been investigated for target detection from hyperspectral remote sensing data. The efficacy of algorithms has been examined over two different hyperspectral datasets which include a synthetic image and an AVIRIS image. The quality of target detection from these algorithms has been evaluated through visual interpretation as well as through receiver operating characteristic (ROC) curves. The performance of OSP algorithm has been found to be better than or comparable to CEM algorithm. However, KOSP outperforms both the algorithms.

Keywords: Hyperspectral images, target detection receiver operating characteristic

1. INTRODUCTION

Hyperspectral images portray a continuous spectrum of each pixel by capturing the data in several narrow and contiguous spectral bands. This makes them possible to discriminate among various targets on earth surface. Typically, a detection problem can be formulated either as anomaly detection or target detection. An anomaly in a dataset has a different unknown spectral response as compared to the pixels in its neighbourhood and generally has a small spatial extent with low probability of occurrence. As anomaly detection is an unsupervised way of detecting these rare and scare objects, it requires no a priori knowledge about the image or the object to be detected. It may however signify that the detected anomaly may or may not be a target of interest. On the contrary, target detection is a supervised way of detecting small and rare objects from the hyperspectral image. The objective of which is to detect a specific target in a given image assuming that the spectral signature of the target, also called reference signature, is known from other sources such as the spectral library, reference data, field data or the image itself[1,2].

From amongst a number of target detection algorithms in vogue, some are based on linear unmixing of endmembers present in the scene, which require complete knowledge of image endmembers. These may be limited by the determination of an appropriate number of endmembers present in the scene.

Alternatively, some algorithms require the knowledge of only target endmembers.

A set of other algorithms such as independent component analysis (ICA) aims to find a linear representation of non-Gaussian data so that the components (constituting components of an image) are statistically independent. Further, the ICA does not require any priori information about the targets and may still be able to segment independent sources, thus, detecting small and even camouflage targets. Yet some other target detection algorithms may be nonlinear that make use of kernel functions. The main aim of this paper is to provide a comparative assessment of a few target detection algorithms. These include OSP, CEM, and KOSP algorithms.

2. ORTHOGONAL SUBSPACE PROJECTION ALGORITHM

Target detection using orthogonal subspace projection (OSP) is an extension of OSP based classification of hyperspectral data in which the spectral signatures of interest (i.e., of target) act as the desired signature and the other spectral signatures (i.e., of background) in the image act as the undesired signatures. The ultimate goal of the OSP is to suppress the undesired signatures in the output image and highlight the desired signature (i.e., the targets in a target detection problem).

Typically, at the spatial resolution of a hyperspectral image, a single pixel may include multiple classes (i.e., it may be a mixed pixel). Thus, the spectral signature of a single pixel may be the average of the spectral signature of various classes (endmembers) present in the pixel.

Mathematically, a hyperspectral image can be considered as a (b x N) matrix $\mathbf{X} = \{\mathbf{x}_1, \mathbf{x}_{2...}\ \mathbf{x}_N\}$, where N is the total number of pixels in the image and b is the total number of spectral bands. $\mathbf{x}_i = \{\mathbf{x}_{i1}, \mathbf{x}_{i2},….\mathbf{x}_{ib}\}^T$ is a (b x 1) vector corresponding to the ith mixed pixel in the image. Using linear mixture model, each pixel $\mathbf{x}_i$ can be modeled as a linear combination of the endmembers present in the pixel. Mathematically, it can be expressed as,

$$\mathbf{x} = \mathbf{M}\boldsymbol{\alpha} + \mathbf{n} \qquad (1)$$

where $\mathbf{M} = \{\mathbf{m}_1, \mathbf{m}_2, ……, \mathbf{m}_p\}$ is a (b x p) matrix of spectral signatures of p endmembers in the image and $\mathbf{m}_i = \{\mathbf{m}_{i1}, \mathbf{m}_{i2},….\mathbf{m}_{ib}\}^T$ is a (b x 1) vector corresponding to the ith endmember spectral signature, $\boldsymbol{\alpha} = \{\alpha_1, \alpha_2,…., \alpha_p\}^T$ is a (p x 1) vector in which α_j corresponds to the fraction of the jth endmember present in the pixel. $\mathbf{n}$ is the (b x 1) vector representing the random noise, which is assumed to be an additive Gaussian white noise with zero mean and a covariance matrix of $\sigma^2\mathbf{I}$ (with σ^2 is the variance of the noise) and $\mathbf{I}$ is the (b x b) identity matrix.

When the objective is to detect a particular target with spectral signature $\mathbf{d}$, the remaining signatures can be considered as undesired. Let $\mathbf{U}$ be the matrix corresponding to the undesired spectral signatures, then $\mathbf{M}\boldsymbol{\alpha}$ for each pixel vector $\mathbf{x}$ can be broken as[3],

$$\mathbf{x} = \mathbf{d}\alpha_d + \mathbf{U}\boldsymbol{\alpha}_U + \mathbf{n} \qquad (2)$$

where $\mathbf{d}$ is a (b x 1) spectral signature corresponding to the target of interest and α_d is a (1 x 1) fraction of target in the pixel $\mathbf{x}$. $\mathbf{U}$ is a (b x p-1) matrix corresponding to the spectral signatures of the remaining p-1 undesired endmembers and $\boldsymbol{\alpha}_U$ is a (p-1 x 1) vector, which corresponds to the fractions of p-1 undesired signatures in the pixel $\mathbf{x}$.

The effect of undesired signatures $\mathbf{U}$ can be eliminated by developing an operator $\mathbf{P}$, which projects the pixel vector $\mathbf{x}$ in a subspace that is orthogonal to the vectors of $\mathbf{U}$. This projected vector nullifies the effect of signatures in $\mathbf{U}$ and corresponds to the energy of the desired signature and the noise. The least square optimal rejection operator $\mathbf{P}$ is a (b x b) matrix given as[4],

$$\mathbf{P} = \mathbf{I} - \mathbf{U}\mathbf{U}^\# \qquad (3)$$

where $\mathbf{U}^\# = (\mathbf{U}^T\mathbf{U})^{-1}\mathbf{U}^T$ is the pseudoinverse of $\mathbf{U}$.

After applying P, Eqn (2) reduces to,

$$\mathbf{P}\mathbf{x} = \mathbf{P}\mathbf{d}\alpha_d + \mathbf{P}\mathbf{n} \qquad (4)$$

Once the background is supressed, the next step is to maximize the signal to noise ratio, Let $\mathbf{r}^T$ be a (1 x b) operator that maximizes the signal to noise ratio which is given as,

$$\mathbf{r}^T = \beta\mathbf{d}^T \qquad (5)$$

here, $\beta = 1$. Thus, the detection operator for the desired target signature in the presence of white Gaussian noise and the undesired background signatures is given by a (1 x b) vector $\mathbf{w}^T$,

$$\mathbf{w}^T = \mathbf{d}^T\mathbf{P} \qquad (6)$$

The detection operator is applied to each pixel in the image resulting in a scalar quantity for each pixel. The scalar quantity has higher values for the pixels, where the target is

located in the image and lower values for the pixels which correspond to the background so that in the resulting gray scale image the target pixels have higher brightness as compared to the background pixels.

3. CONSTRAINED ENERGY MINIMIZATION ALGORITHM

The OSP algorithm for target detection is based on the assumption that complete knowledge of image endmembers (target as well as background) is known, which may practically be difficult. Constrained energy minimization (CEM) algorithm focuses only on the desired signature (i.e., of target) and neither on the background signature nor noise in the image.

The CEM algorithm imposes a constraint on the desired signature while minimizing the interfering effects caused by the undesired (background) as well as the unknown signal sources. Since, it is assumed that only the desired target signature is known, the undesired signatures and the noise are suppressed in terms of their energies[5]. The objective of the CEM is to design a finite impulse response (FIR) linear filter with b filter coefficients $\{w_1, w_{2........} w_b\}$, denoted by a b dimensional vector $\mathbf{w} = \{w_1, w_{2........} w_b\}^T$ that minimize the filter output energy corresponding to the constraint,

$$\mathbf{d}^T\mathbf{w} = \mathbf{w}^T\mathbf{d} = 1 \qquad (7)$$

The CEM has been developed to solve the linearly constrained optimization problem given as,

$$\min_{w} \left\{ w^T K\, w \right\} \text{ subject to } \mathbf{d}^T\mathbf{w} = \mathbf{w}^T\mathbf{d} = 1 \qquad (8)$$

where $K = \left[\dfrac{1}{N}\sum_{i=1}^{N} x_i x_x{}^T \right]$ is the auto-correlation sample matrix of the image. The optimal solution to Eqn (8) is given by[6],

$$\mathbf{w}' = \dfrac{K^{-1}\,d}{d^T\,K^{-1}\,d} \qquad (9)$$

with the optimal weight vector $\mathbf{w}'$, the CEM filter can be obtained by,

$$\mathbf{CEM(x)} = (\mathbf{w}')^T\mathbf{x} = \left(\dfrac{K^{-1}\,d}{d^T\,K^{-1}\,d} \right)^T x = \dfrac{d^T\,K^{-1}\,x}{d^T\,K^{-1}\,d} \qquad (10)$$

Similar to the OSP algorithm, the operator obtained in Eqn (10) is applied on each pixel in the input image which results in a grey scale image in which the brighter pixels corresponds to the target pixels and the darker ones correspond to the background pixels.

4. KERNEL ORTHOGONAL SUBSPACE PROJECTION ALGORITHM

When the classes in the original space are not linearly separable, an appropriate non-linear mapping may be applied to transform the data in much higher dimensional space where the classes become linearly separable and hence can be classified using a linear classifier. However, the application of linear algorithm is not feasible in the transformed space because of the high dimensionality; therefore, the original linear algorithm is kernelized by using the well-known *kernel trick* property of the Mercer kernels, where the linear algorithm in the feature space is reformulated only in terms of inner products of the mapped input data. These inner products are then replaced by the kernel functions that are computed directly in terms of the original

input data. Here, a kernelized OSP algorithm (KOSP), which is equivalent, to a nonlinear version of the OSP algorithm in the original input space has been considered for target detection.

For the detection purpose, the Gaussian radial basis function (RBF) kernel has been selected, which is given by,

$$k\left(v_i, v_j\right) = \exp\left(\left(\| v_i - v_j \|^2\right)/h\right) \tag{11}$$

where $h \varepsilon R$ (the set of real numbers) and represents the width of the Gaussian distribution.

The reason for selecting the Gaussian RBF kernel is its translation invariant nature and smoothness of the associated nonlinear map. The translation invariant property ensures the robust detection performance since it depends on the difference between spectral vectors therefore even if the spectral signatures are subject to irregular illumination conditions, it does not make a difference in the detection performance. The smoothness of the associated nonlinear map implies that topographic ordering of the data in the original input space is preserved in the mapped feature space.

The detection operator as derived in Eqn (6) for target detection using OSP algorithm is given as $\mathbf{w}^T = \mathbf{d}^T\mathbf{P}$. Using the singular value decomposition of $\mathbf{U} = \mathbf{S}\sum\mathbf{V}^T$ where $\mathbf{S}$ is the eigenvectors of $\mathbf{UU}^T = \mathbf{S}\sum\sum^T\mathbf{S}^T$ and V is the eigenvectors of $\mathbf{U}^T\mathbf{U} = \mathbf{V}\sum^T \sum\mathbf{V}^T$. Thus the rejection operator given in Eqn (3) can be rewritten as

$$\mathbf{P} = \mathbf{I} - \mathbf{UU}^\# = \mathbf{I} - \mathbf{U}(\mathbf{U}^T\mathbf{U})^{-1}\mathbf{U}^T = \mathbf{I} - \mathbf{SS}^T \tag{12}$$

Thus the OSP algorithm can also be rewritten as

$$\mathbf{w}^T\mathbf{x} = \mathbf{d}^T\mathbf{Px} = \mathbf{d}^T (\mathbf{I} - \mathbf{SS}^T)\mathbf{x} \tag{13}$$

The OSP algorithm in feature space is given as[7],

$$\mathbf{w}_\Phi^T\mathbf{x} = \Phi\left(\mathbf{d}\right)^T \mathbf{I}_\Phi \Phi\left(\mathbf{x}\right) - \Phi\left(\mathbf{d}\right)^T \mathbf{S}_\Phi \mathbf{S}_\Phi^T \Phi\left(\mathbf{x}\right) \tag{14}$$

where Φ is the nonlinear mapping.

The kernelized version of the OSP algorithm in Eqn (14) is given by,

$$\mathbf{w}_\Phi^T\mathbf{x} = K\left(\mathbf{M}_{bd},\mathbf{d}\right)^T \eta\eta^T K\left(\mathbf{M}_{bd},\mathbf{x}\right) - K\left(\mathbf{U},\mathbf{d}\right)^T \beta\beta^T K\left(\mathbf{U},\mathbf{x}\right) \tag{15}$$

where x = pixel vector

K = kernel function

d = desired target signature

$\mathbf{M}_{bd} = (\mathbf{U} \cup \mathbf{d})$ (union of **U** and **d**) where **U** corresponds to the matrix containing all the background signatures

η = a matrix whose columns are the eigenvectors of the centered kernel matrix $K(\mathbf{M}_{bd},\mathbf{M}_{bd})$

In deriving Eqn (15), a centred Gram matrix $\hat{\mathbf{K}}$ can be obtained from an uncentred Gram Matrix **K** by, $\tag{16}$

$$\hat{\mathbf{K}} = \left(\mathbf{K} - 1_N\mathbf{K} - \mathbf{K}1_N + 1_N\mathbf{K}1_N\right)$$

where $(1_N)_{ij} = 1/N$ is an $N \times N$ matrix. Also, the empirical maps $K(\mathbf{M}_{bd},\mathbf{d})$, $K(\mathbf{M}_{bd},\mathbf{x})$, $K(\mathbf{U},\mathbf{d})$, and $K(\mathbf{U},\mathbf{x})$ are centred by removing their corresponding kernel map means. (e.g.

$$\hat{\mathbf{K}}\left(\mathbf{M}_{bd},\mathbf{d}\right) = K\left(\mathbf{M}_{bd},\mathbf{d}\right) - \vec{1}.(1)/\left(p\right)\sum_{i=1}^{p} k\left(r_i,\mathbf{d}\right), r_i \varepsilon \mathbf{M}_{bd}$$

where $\vec{1} = \left(1,1,.....,1\right)^T$, a $N \times 1$ column vector).

Thus, Eqn (15) gives the KOSP algorithm processed output pixel corresponding to each input pixel resulting in a grey scale image in which the brighter pixels corresponds to the target pixels and the darker ones correspond to the background pixels.

5. EXPERIMENTAL DATASETS

Two experimental datasets have been considered to examine the efficacy of the selected target detection algorithms.

5.1 Dataset I: Synthetic Data

The dataset I is a 30 bands synthetic image generated based on the statistics of an actual hyperspectral image and has been obtained from Tiwari[8]. The synthetic image is composed of five different segments each containing one target. Four of these segments measures 140 x 60 pixels and one central segment is made up of 80 x 80 pixels. Thus, the 200 x 200 pixels synthetic image contains five small targets matching
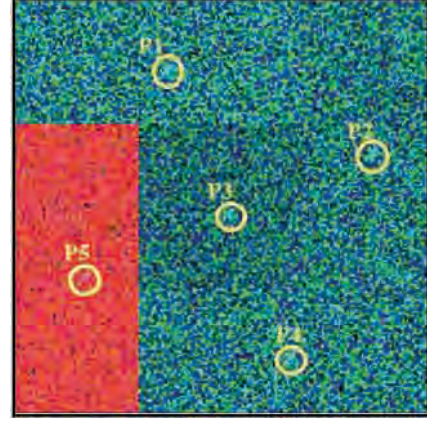

Figure 1. Dataset I: Synthetic image. The encircled areas mark the position of five aircrafts along with the labels[8].

the shape of aircraft (size ~ 18 pixels) centered at (30, 70), (70,170), (170,130), (130, 30) and (100,100) (Fig. 1). These have been labeled as P1 to P5.

A glance at the spectral profiles of the five aircrafts indicates that the spectral characteristics of the targets P1-P4 are similar whereas the target P5 has just opposite spectral characteristics to the others. This may have bearing on the detection of targets using different algorithms. Therefore, the target detection has been performed twice, first for the detection of P1 - P4 targets and then for the detection of P5 target separately. Five background endmembers, named as Back1 through Back5, from each of the five segments have been identified in the image. Only two background endmembers Back 1 and Back 5, having distinct spectral characteristics have been considered further in the experiments on target detection.

5.2 Dataset II: AVIRIS Image

The AVIRIS image is composed of 400 x 400 pixels in 224 bands data at a spatial resolution of 4 meter, acquired over naval air station in San Diego, California. The image has been borrowed from the example datasets in ENVI 4.2 image processing software. Out of the 224 bands, after removing bad bands and water absorption bands, only 189 bands have been used for the analysis. In the present case, the image supplied has already been atmospherically corrected using ENVI's FLAASH module resulting in a reflectance image.

A 286 x 198 pixels subset of the image containing six aircrafts as targets has been extracted with targets centred at

locations (50,30), (69,20), (87,8), (230,134), (243,142), and (197,156) and labelled as P1 to P6 respectively (Fig 2(a)). The total number of pixels constituting the target is not known. Further, since no reference for this dataset is available, the Google Earth image (Fig 2(b)) acquired over the same area has been taken as a reference data for the identification of various background classes present in the image.

From the Google Earth image, four background endmembers, namely, vegetation, buildings and two types of roads, have been identified. A glance at the spectral curves of the six aircrafts indicates that the spectral characteristics of the six targets follow the same trend. Additionally, the spectral characteristics of targets P1 - P3 are almost similar. Thus, to investigate the effect of spectral variability in targets, five cases corresponding to five different target endmembers have been considered for the same background endmembers. These five cases include,

- The target signature taken as an average of signatures of all the target endmembers P1, P4, P5 and P6. This has been named as Pavg
- The target signature of P1
- The target signature of P4
- The target signature of P5
- The target signature of P6

Also, to investigate the behaviour of the algorithm corresponding to the selection of background endmembers, the number of background endmembers have been changed as three (vegetation, buildings, road1), two (vegetation, buildings) and one (vegetation) as separate experiments.

6. RESULTS AND DISCUSSION

6.1 Assessment of OSP Algorithm on Dataset I

As discussed earlier the detection of the targets P1-P4 and P5 has been considered separately. On conducting experiments for the detection of P1-P4 with Back1 and Back5 as background endmembers, all the five targets (shown in Fig. 3(a)) appear suppressed as the spectral signature of Back1 is similar to that of P1-P4. Further, P5 is not detected due to its similar spectral signature with that of Back5. Thus, for the detection of targets P1-P4, only Back5 has been used as background endmember. (Figs. 3(b) - 3(c)). This has resulted in detection of all the targets P1-P4, with 100% detection rate and no false alarms.

(a)

Figure 2. (a) Dataset II: Subset of a true color (R: 28, G: 19 and B: 10) image extracted from AVIRIS image acquired over San Diego area. The encircled areas show the location of six targets (aircrafts) (b) A portion of Google Earth image.
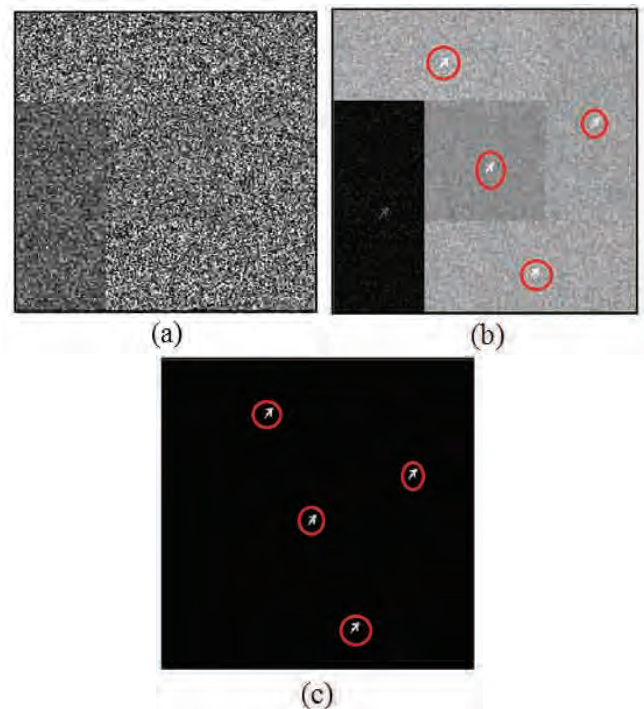

Figure 3. Grey scale outputs from OSP algorithm for the detection of P1-P4 in dataset I using (a) Back1 and Back5 (b) Back5, as background endmembers. (c) Binary outputs for detection of P1 using Back5 background endmember. The encircled areas mark the detected targets.

Similarly, when the experiment has been conducted for the detection of target P5 with Back1 and Back5 as the background endmembers, all the targets have been suppressed (shown in Fig.4(a)) leading to no detection. Hence, for the detection of P5, only Back1 has been used as background endmember. However, the target P5 (Fig. 4(b)) still has not been detected.
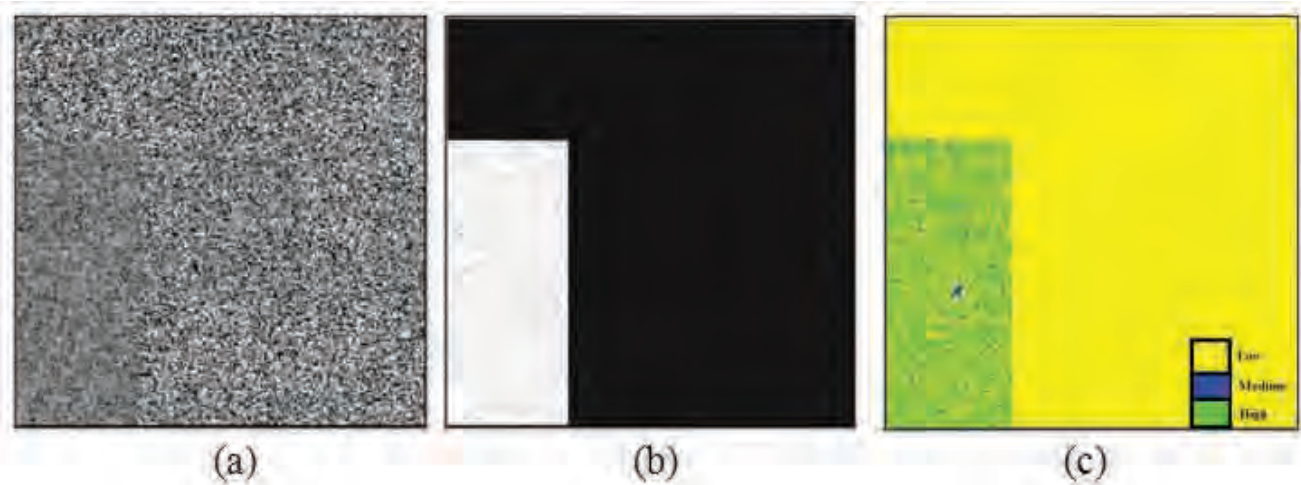
Figure 4. Grey scale outputs from OSP for detection of P5 in dataset I using (a) Back1 and Back5 (b) Back5, as background endmembers. (c) Pseudo colour image corresponding to (b).

This may be due to the fact that spectral characteristics of Back1 and P5 are similar.

This can further be illustrated from the pseudo color image of the output (Fig.4(c)) where the pixels with output values (obtained as a result from the application of OSP algorithm) less than that of the target has been assigned yellow color and those equal to and higher than the targets have been assigned blue and green colors, respectively. It is clear from the pseudo colored image that background in the four segments corresponding to targets P1-P4 is completely suppressed. The ROC curves for detection of these two categories of targets are shown in Fig. 5.
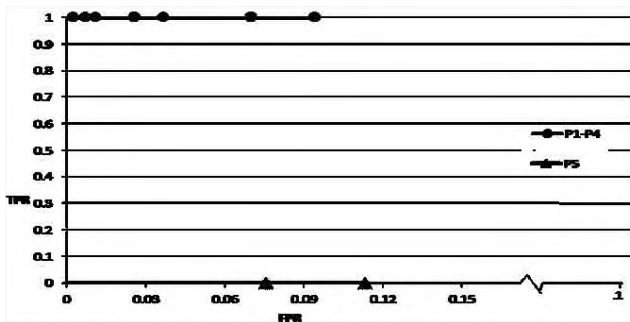
Figure 5. ROC curves for the outputs from OSP for detection of targets P1-P4 and P5.

A glance on the ROC curves also verifies the 100% detection rate and 0% false alarm rate in case of detection of the targets P1-P4 and 0% detection rate in case of detection of target P5. jdk.

6.2 Assessment of OSP Algorithm on Dataset II

Five cases as discussed earlier have been considered while detecting the targets in dataset II. Figures 6 and 7 show the binary images and the ROC curves corresponding to these experiments.

These binary images and the corresponding ROC curves signify that the detection performance is very much similar in all the cases and is about more than 80% of detection rate at a false alarm rate of 7-8%. This indicates that spectral variability among the targets in this dataset is not an issue. Thus, the

average of target endmembers Pavg, has been taken as the spectral endmember representing the target class for further analysis of the algorithm on this dataset.

In order to analyse the impact of background endmembers on the detection algorithm, the number of background endmembers have been changed as three (vegetation, buildings, road1), two (vegetation, buildings) and one (vegetation) separately with the target endmember taken as an average of spectral signatures of all the targets. The binary images thus produced from OSP algorithm for the four cases are shown in Figs. 8 (a) - 8(d).

A glance at these binary outputs and the corresponding ROC curves in Fig. 9 indicates that targets have been detected in all the cases but with different values of false alarm rates (i.e., with different accuracy). The least false alarm rate has been observed when the background endmembers have been considered separately. This may be attributed to the fact the background classes have been considered separately, which resulted in sufficient suppression of the background thereby highlighting the targets. In other cases, when the number of background endmembers were decreased to 2, 3, or 4, the background classes could not be suppressed, which resulted in large number of false alarms.

Further, an additional target (a very small aircraft) encircled by dotted line in the binary output (Fig. 8 (d) has also been detected, which in fact has not been visible in the original image. The OSP, however, has been successful in detecting this invisible target in the binary output.

6.3 Assessment of CEM Algorithm on Dataset I

The CEM algorithm produced the same binary image obtained is output as shown in Fig. 10 while considering the targets P1-P4 and P5 separately. The ROC curves produced from CEM for the detection of two types of targets are shown in Fig. 11. The ROC curves do not show false alarm rate of value 0 because as shown in Fig. 10 in detection of P1-P4, the pixels corresponding to P5 has occurred as false alarms and in detection of P5, the pixels corresponding to P1-P4 have occurred as false alarms.
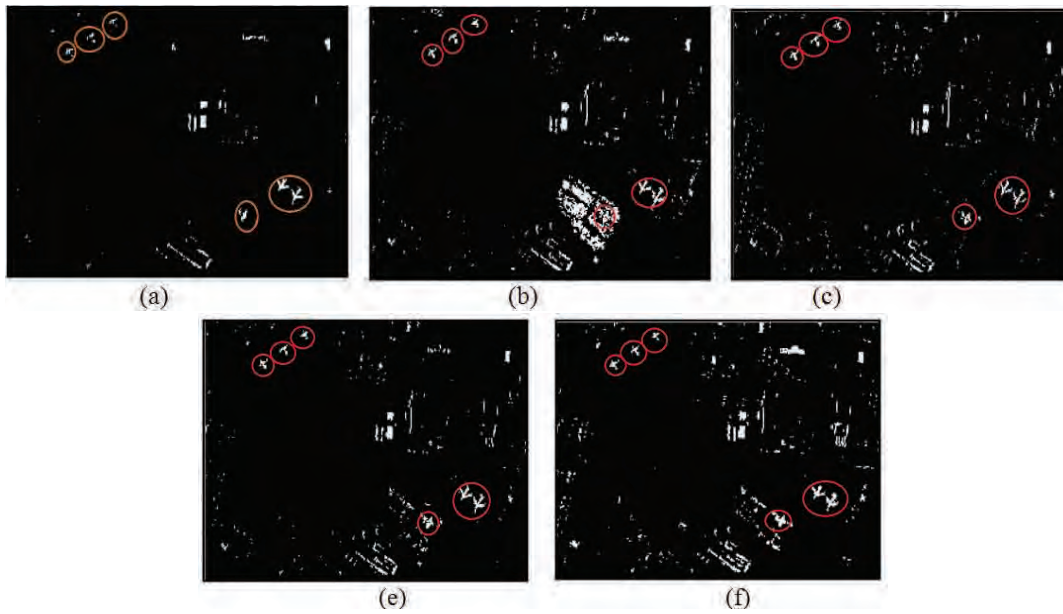
Figure 6. Binary images obtained from the OSP algorithm implemented on dataset II corresponding to target endmembers (a) Pavg, (b) P1, (c) P4, (d) P5, and (e) P6. The encircled areas mark the detected targets.
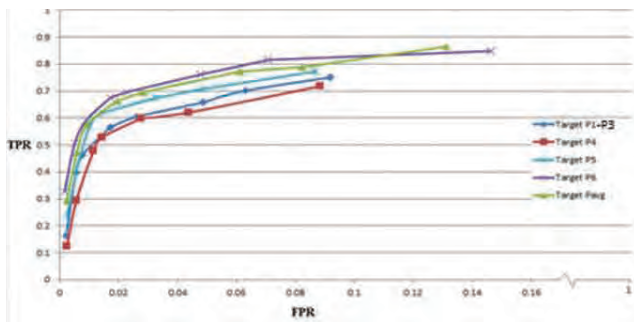

Figure 7. The ROC curves for the outputs from OSP on dataset II corresponding to target endmember (a) P1, (b) P4 , (c) P5, (d) P6, and (e) Pavg.
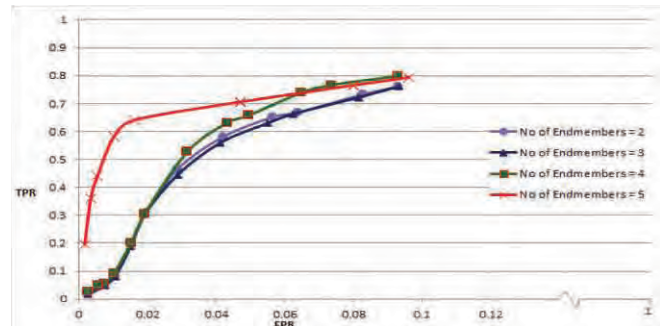

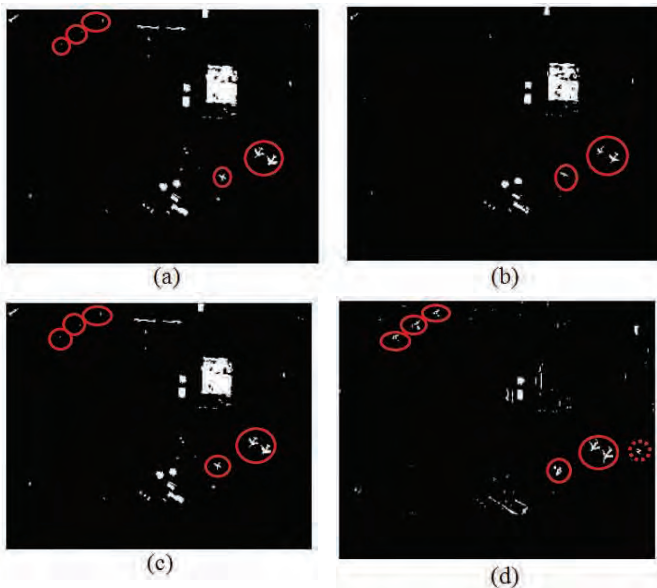**Figure 9. ROC curves for the outputs from OSP on dataset II for different number.of end members.**

Figure 8. Binary images from the OSP algorithm implemented on dataset II for different number of endmembers : 2 in (a), 3 in (b), 4 in (c), and 5 in (d).
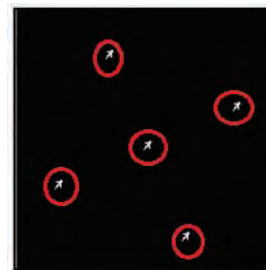
Figure 10. Binary image from CEM corresponding to targets P1-P4 and P5 taken separately. The encircled areas mark the detected targets.
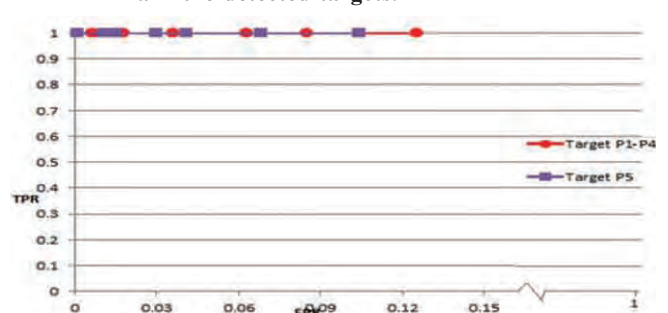

Figure 11. ROC curves for the outputs from CEM on dataset I for different target signatures

6.4 Assessment of CEM Algorithm on Dataset II

The binary outputs obtained as a result corresponding to all the five cases mentioned in earlier section, using CEM algorithm are shown in Fig. 12. The binary outputs show that all the targets have been detected by the CEM algorithm in all the cases. The analysis of the corresponding ROC curves shown in Fig. 13 reflects that detection and false alarm rate are almost similar in all the cases. It shows that spectral variability of the targets in dataset II has no bearing on the detection performance. The reason being the spectral separation between the target and background classes is high for this dataset.

6.5 Assessment of KOSP Algorithm on Dataset I

In both the cases, the binary images obtained from KOSP have been shown in Fig. 14. The corresponding ROC curves for the detection of two types of targets have been shown in Fig. 15.

The width of the RBF kernel has been determined experimentally which for dataset I has been chosen as 61e+7. The binary images and the corresponding ROC curves justify the fact that in both the cases the targets have been detected with 100% true detection and 0% false alarm rate. This ideal detection is possible only due to increased separation between the target and the background classes caused by nonlinear transformation of the original high dimensional data into much higher dimensional space.

6.6 Assessment of KOSP Algorithm on Dataset II

As discussed in earlier section, the experiments have been conducted to evaluate the performance of this algorithm corresponding to the spectral variability of the targets. The endmembers for these experiments have already been discussed. Figures 16 and 17 show the binary images and
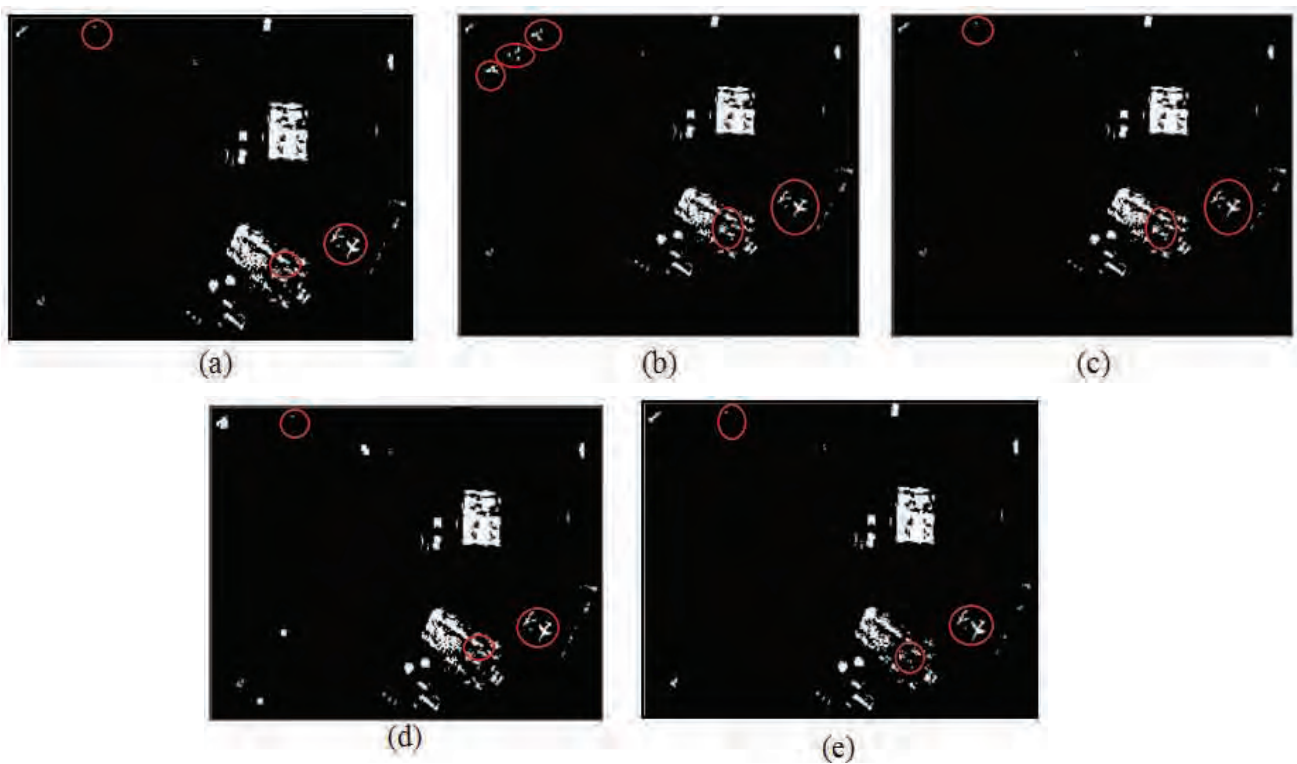

Figure 12. Binary images from CEM on dataset II for target endmember (a) P1, (b) P4, (c) P5, (d) P6, and (e) Pavg. The encircled areas mark the detected targets
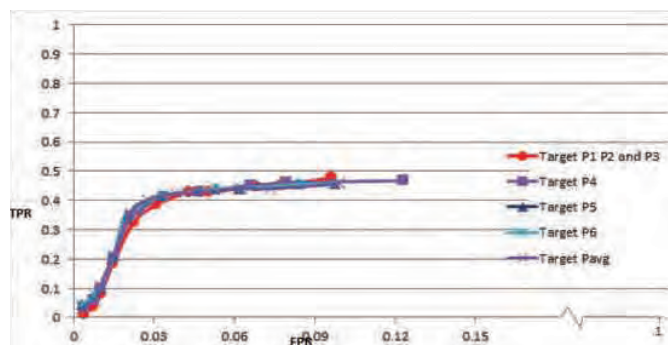

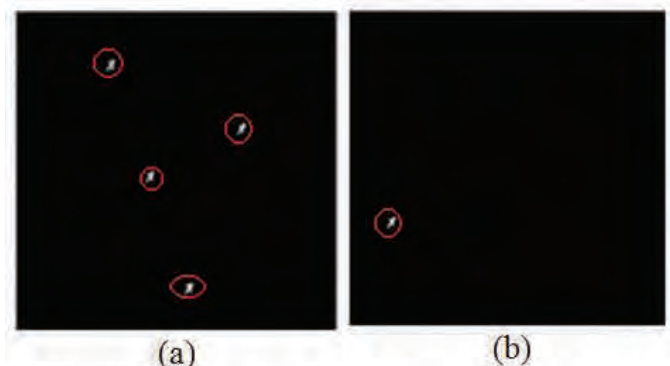**Figure 13. ROC curves for the outputs from CEM on dataset II for different target endmember**

Figure 14. Binary images from KOSP on dataset I for targets (a) P1-P4, (b) P5.
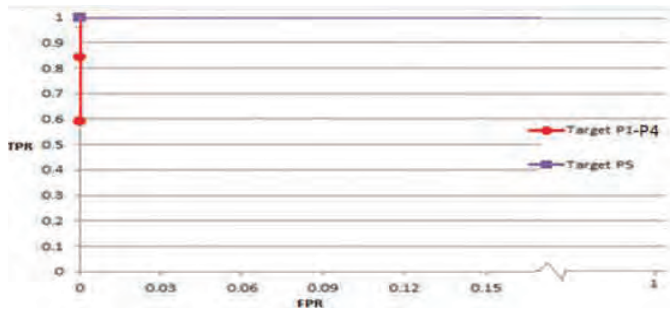
Figure 15. ROC curves for the outputs from KOSP on dataset I

has yielded the highest detection accuracy due to increased separation between the target and background classes in the higher transformed space. OSP has not been able to detect the target P5 because of the less separation between P5 and the background class Back1. However, CEM has been able to detect both the targets but with some false alarms.

Further, OSP has shown accurate detection on Dataset II by suppressing the background classes in the image and highlighting the targets. However, the performance of the CEM and KOSP algorithms is comparable for Dataset II. The KOSP has not been able to perform well for both the dataset. One of the reasons may be attributed to the inappropriate selection of the kernel parameter.
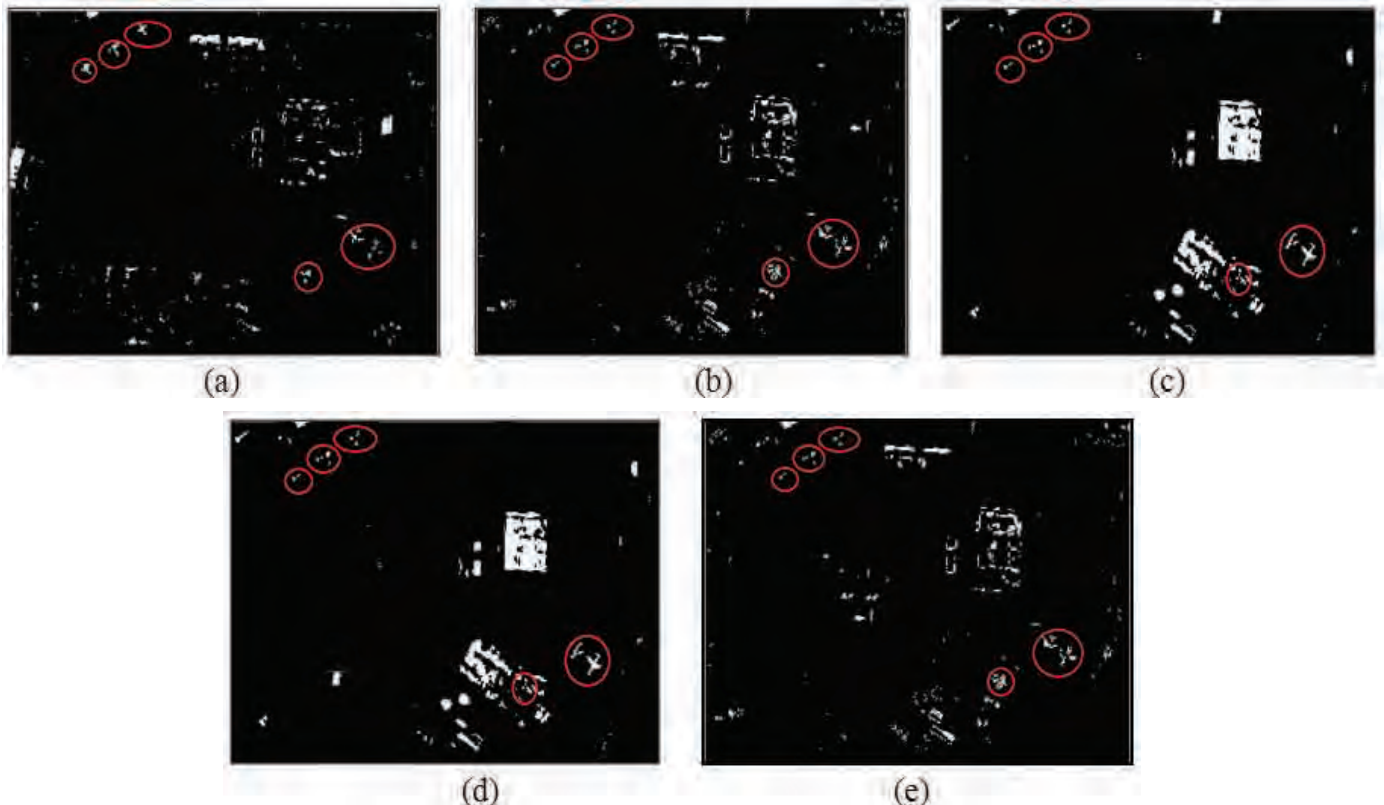

Figure 16. Binary images obtained from KOSP on Dataset II corresponding to target endmember (a) Pavg, (b) P1, (c) P4, (d) P5, and (e) P6. The encircled areas mark the detected targets.

the ROC curves corresponding to these experiments. After a number of experiments with KOSP on dataset II, the width of the RBF kernel has been selected as 20e+7.

The outputs obtained for this dataset show that all the targets have been detected by KOSP. The ROC curve shows less detection rate for lesser false alarm rate because of miss-detection of the targets P4-P6 at increased threshold values. These ROC curves also justify that the detection performance is very much similar when the target endmembers have been considered individually or an average of them has been taken. This signifies that spectral variability among the targets in this dataset is not an issue.

7. COMPARATIVE EVALUATION OF TARGET DETECTION ALGORITHMS

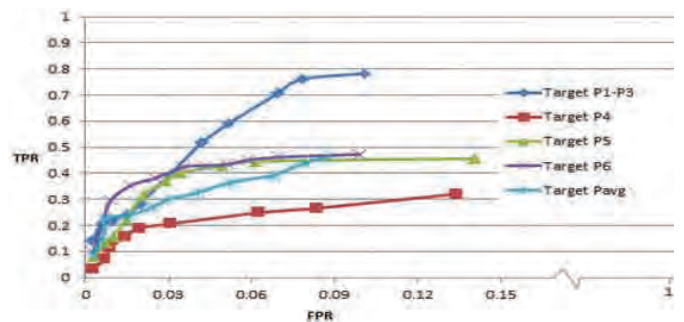Among all the algorithms implemented on Dataset I, KOSP

Figure 17. ROC curves for the outputs from KOSP on dataset II corresponding to target endmember (a) P1, (b) P4, (c) P5, (d) P6, and (e) Pavg.

Further, all the three algorithms have been evaluated comparatively on each dataset individually, for their performance by making the use of ROC curves. A careful evaluation of the ROC curves in Fig.18 shows that OSP has resulted either comparable or higher detection accuracy than the CEM on all the datasets. KOSP has performed better than OSP for Dataset I. The reason for higher performance of KOSP is the detection of targets in much higher dimensional space. For Dataset II the performance of the KOSP has been found to be inferior to that of OSP; this may be due to the improper selection of the parameter which represents the width of the Gaussian RBF kernel. However, one particular case in which CEM has shown a better performance than OSP is in the detection of target P5 in Dataset I. This is due to the similarity of this target to its background, which suppresses the target P5 in background during OSP based target detection, resulting in no true detection at all.
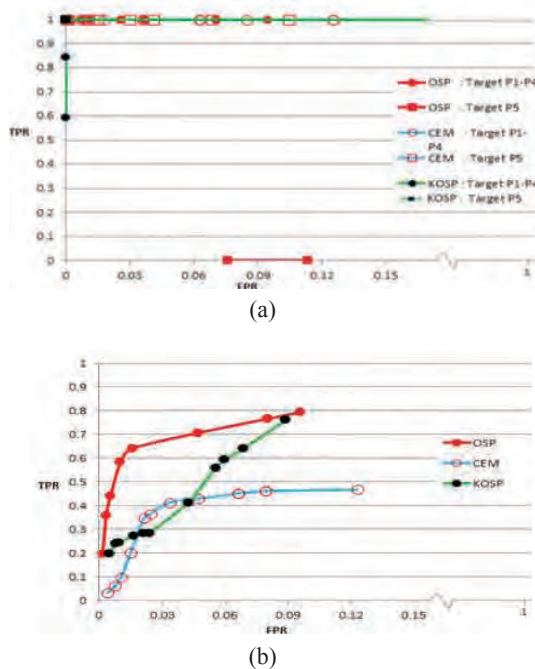

(a)

(b)

Figure 18. Comparative assessment of target detection algorithms on (a) Dataset I, (b) Dataset II, and (c) Dataset III.

8. CONCLUSION

For the target detection algorithms, the spectral variability does matter when the separation between the background and the target class is very less. While using OSP for target detection, it has been observed that the identification of sufficient number of background classes in the image has bearing on the detection rate of the targets. Therefore, these must be selected judiciously. The performance of OSP has been found to be better than or comparable to CEM, because it suppresses the background prior to the detection of targets. However, when the separation between the target and the background class is very less CEM may outperform the OSP algorithm. KOSP algorithm performs better than OSP algorithm. But, the main difficulty in implementing this algorithm lies in the selection of appropriate value of the width of the kernel function. All the

algorithms discussed are robust enough to detect those pixels as anomaly or target which either contain complete or a fraction of the anomaly or target. The width of the Gaussian RBF kernel in KOSP is determined experimentally, the domain of which is the entire set of real numbers. Thus, the development of an appropriate technique for deciding criteria to select an appropriate value for this parameter of kernel function is a great requirement.

REFERENCES

1. Matteoli, S.; Diani, M. & Corsini, G. A tutorial overview of anomaly detection in hyperspectral images. *IEEE Aerospace Electronic Syst. Magazine*, 2010, **25**(7-2), 5-28.
2. Matteoli, S.; Diani, M. & Corsini, G. Hyperspectral anomaly detection with kurtosis-driven local covariance matrix corruption mitigation. *IEEE Geosci. Remote Sens. Letters*, 2011, **8**(3), 532-36.
3. Chang, C.-I. Orthogonal subspace projection (OSP) revisited: A comprehensive study and analysis. *IEEE Trans. Geosci. Remote Sens.*, 2005, **43**(3), 502-518.
4. Harsanyi, J. C. & Chang, C.-I. Hyperspectral image classification and dimensionality reduction: An orthogonal subspace projection approach. *IEEE Trans. Geosci. Remote Sens.*, 1994, **32**(4), 779-785.
5. Chang, C.-I. Recent advances in hyperspectral signal and image processing. Transworld Research Network, 2006, 146-169.
6. Harsanyi, J.C.; Farrand, W. & Chang, C-I. Detection of subpixel signatures in hyperspectral image sequences. *In* Proceedings of American Society of Photogrammetry and Remote Sensing, 1994, Reno, NV, 236-247.
7. Kwon, H. & Nasrabadi, N. M. Kernel orthogonal subspace projection for hyperspectral signal classification. *IEEE Trans. Geosci. Remote Sens.*, 2005, **43**(12), 2952-2962.
8. Tiwari, K.C. Target detection using optical and microwave remote sensing. Indian Institute of Technology Roorkee, 2007. PhD thesis.

Contributors

Prof. Manoj K. Arora obtained his BE (Civil Engineering) from PEC Chandigarh, ME (Survey and Photogrammetry) from University of Roorkee and PhD (Remote Sensing) from University of Wales Swansea (UK) in 1984, 1986 and 1996 respectively. Currently working as Professor of Geomatics Engineering in the Department of Civil Engineering. He has published about 180 research papers in reputed journals and conference proceedings. He has guided 11 Doctoral and 50 Master's theses, has published two books. His research interests include: Remote sensing and GIS, digital image processing, land cover mapping and disaster management applications.

Ms Shweta Bansal graduated in computer science and engineering from VIET in 2008 and MTech (Civil) from IIT Roorkee in 2010. Currently she is working as a software engineer at EDA company Atrenta Pvt Limited, Noida. Her research interests include:Multispectral and hyperspectral image analysis, image processing, detection of small and rare objects using hyperspectral remote sensing.

Dr Sangeeta Khare received her MSc (Mathematics) from Allahabad University and PhD (Mathematics) from Indian Institute of Technology Kanpur. She is working currently as Scientist 'G' in Image Analysis Center of Defence Electronics Applications Laboratory, Dehradun. Her current research interest include development of techniques and software for Hyper spectral data processing and high level analysis of satellite images as well as application of soft computing in image analysis.

Kiran Chauhan
(Bio-data is not available)